

Experimental Measurements of Turbulent Junction Flow Using High Speed Stereo PIV and IR Thermography

Syed S. Elahi ¹, Eric A. Lange ² and Stephen P. Lynch ³
The Pennsylvania State University, University Park, PA, 16802

Turbulent junction flow is commonly seen in various turbomachinery components, heat exchangers, submarine appendages, and wing-fuselage attachments, where the approach boundary layer separates and rolls up into a coherent system of vortices upstream of a bluff body. The highly unsteady behavior of this flow causes high pressure fluctuations on the wall, and if the fluid temperature is different than the wall temperature, also causes high heat transfer. One of the signature features of these flows is a bimodal distribution of velocity around the vortex system. In this paper, the flow physics as well as heat transfer of the turbulent junction flow are investigated using PIV and IR measurements respectively. Among the three objectives of this paper, the first one is to demonstrate the unique experimental setup that captures temporally resolved turbulent flow-field measurements. The second objective is to analyze the dynamics of primary vortex for various Reynolds numbers. The final objective is to investigate the effect of the unsteady junction flow on the endwall heat transfer.

Nomenclature

Re_T – Body thickness Reynolds number, $(\frac{U_{ref} T}{\nu})$

C – Chord length

DES – Detached Eddy Simulation

Y – Direction normal to the endwall

Z – Direction across the tunnel

U_{ref} – Freestream velocity

HS – Horseshoe

IR – Infrared

u^* – Inner coordinate velocity $(\sqrt{\frac{\pi_{wall}}{\rho}})$

y^+ – Inner coordinate $(\frac{y^* u^*}{\nu})$

LDV – Laser Doppler velocimetry

St_x – Local Stanton number $(\frac{h}{\rho c_p U_{ref}})$

Re_θ – Momentum thickness Reynolds number, $(\frac{U_{ref} \theta}{\nu})$

MDF – Momentum Deficit Factor $(Re_T)^2 (\theta/T)$

T – Maximum Rood wing body thickness

δ^*/T – Nondimensional boundary layer thickness

δ^*/T – Nondimensional displacement thickness

θ/T – Nondimensional momentum thickness

f_{nd} – Nondimensional sampling frequency (f^*)

$RANS$ – Reynolds-Averaged Navier Stokes

C_p – Pressure coefficient

C_f – Skin friction coefficient

S – Span

X – Streamwise direction

Tu – Turbulence intensity

¹ Graduate research assistant, Mechanical and Nuclear Engineering.

² Graduate research assistant, Mechanical and Nuclear Engineering.

³ Assistant professor, Mechanical and Nuclear Engineering, AIAA Senior Member.

I. Introduction

Turbulent junction flow is a phenomenon that is often observed in turbomachinery components, wing-fuselage attachments on aircrafts, fin-tube interfaces of heat exchangers, bridge piers, and submarine appendages. It is generally well-understood that turbulent junction flow causes high surface heat transfer near the junction. This rise in surface or endwall heat transfer severely affects the performance of hot-section turbomachinery components such as first-stage turbine vanes and blades. Han et al. [1] reported that a variation of 25°C in the incoming flow (where nominal gas temperature is 1800°C) for hot-section turbine parts can reduce the part life by half. A turbulent junction flow or horseshoe (HS) vortex system occurs when a turbulent boundary layer on a wall encounters a bluff body, which causes the turbulent boundary layer to separate from the wall and reorganize into coherent vorticity. The size and dynamics of the HS vortex system is dependent upon the angle of attack of a wing, Reynolds number, the size of the body, and inlet boundary conditions. This flow is well-known to be highly unsteady, which leads to high pressure fluctuations around the vortex location. In addition, convective heat transfer near the junction due to the HS vortex can be up to 200% greater than in the boundary layer upstream [2]. The turbulence intensities are also reported to be high in this type of flow [3]. In this paper, an experimental setup is presented which is designed to capture the time-resolved junction flow in front of a common research wing geometry, also known as the Rood wing [4]. Experimental measurements of the junction flow are captured with a high speed stereo particle image velocimetry (SPIV) system, which provides three components of velocity in a plane at kHz sampling rates. Time-averaged data are compared to previous measurements [4] of junction flow, and the temporally resolved dataset are analyzed for dynamic behaviors over a wide range of Reynolds numbers. Finally, convective heat transfer around the junction is presented and explained using the flowfield measurements.

II. Previous Studies

Junction flow is a frequently studied topic in fluid mechanics and heat transfer due to its relevance in many engineering applications. Devenport and Simpson [4] studied the endwall flow behavior of the HS vortex in front of a Rood wing (3:2 semi-elliptical leading edge connected at the maximum thickness with NACA0020 trailing edge). Time mean measurements of the HS vortex identified two regions of distinct behavior; an upstream region of moderate turbulence stresses and a more intense region of turbulence stresses near the endwall junction. These increases in turbulence stresses were determined to be the product of bi-stable velocity fluctuations, suggesting that the HS vortex exists in two quasi-steady modes, the coherent “backflow mode” near the junction and the more chaotic “zero-flow mode”. Time mean measurements of the heat transfer augmentation effect caused by the HS vortex were undertaken by Lewis et al. [5] and by Praisner and Smith [2,6]. Lewis et al. [5] measured mean heat flux on heated wing/endwall junctions for several wing shapes, finding that the presence of the HS vortex enhanced heat transfer due to the high levels of turbulent stresses found between the separation line and the region upstream of the time mean vortex center, with the maximum heat transfer augmentation right at the junction. Lewis et al. [5] did not find any bimodal behavior in PDF’s of heat flux in the junction flow region of the Rood wing, and thus he was unable to complement the bimodal flow behavior seen by Devenport and Simpson [4]. Praisner and Smith [6] produced contours of time-mean Stanton number on the endwall in front of a Rood wing that showed two distinct bands of high heat transfer associated with the two quasi-steady modes observed by Devenport and Simpson [4]. Time-mean vorticity contours provided a direct correlation between mean heat transfer augmentation and quasi-steady behavior of the HS vortex. Computational studies, such as those by Paik et al. [7] and Yakhot et al. [8] had further supported the existence of quasi-steady modes in the vortex behavior in front of bluff bodies; however, most numerical studies were unable to correctly predict the time-mean vortex core location. Very recent studies on junction flow with cylindrical bodies by Apsilidis et al. [9] and Chen et al. [10] reported a third mode called “intermediate mode” which persisted between the “backflow mode” and “zero-flow mode.”

Time-resolved measurements and simulations of the HS vortex have been the focus of many recent studies in turbulent junction flow and have attempted to gain a greater understanding of the transition between the quasi-steady modes of the HS vortex. Hydrogen-bubble flow visualization and laser velocimetry were used by Kim et al. [11] in a water tunnel to analyze the unsteady vortex behavior in front of a cylinder. Kim et al. [11] identified the formation of strong primary and secondary vortices rotating in the same direction, with a weaker tertiary counter rotating vortex between them. Disturbances caused by separation upstream of the vortices led to acceleration of flow and instability around the primary and secondary vortices. Further details of the transition between quasi-stable states were provided in a numerical study by Paik et al. [7] in which the conditions of Devenport and Simpson’s [4] experiment were closely matched. While there was discrepancy between RANS and DES predictions of the location of the mean HS vortex core, Paik et al. [7] showed that DES predicted the cyclical transition between backflow and

zero-flow modes, which occurred due to the generation of hairpin vortices in front of the HS vortex. These hairpin vortices deconstructed the HS vortex in its coherent backflow mode to form its more chaotic zero-flow mode. Escauriaza and Sotiropoulos [12] also simulated the HS vortex using DES analysis on HS vortex at an order of magnitude lower Reynolds number (2.0×10^4) than in the experiment of Devenport and Simpson [4]. At this lower Reynolds number, mean flow and coherent dynamics of turbulent HS vortex varied significantly from Devenport and Simpson [4]. Previous research by Fleming et al. [13] and Ballio et al. [14] aimed to find the consequences of changing bluff body thickness. Both of these efforts concluded that in the turbulent regime, the dynamics of HS vortex mainly depended on the maximum bluff body thickness and the adverse pressure gradient caused by it.

Other studies attempted to link the unsteady velocity behavior of the HS vortex with time-resolved heat transfer observation on junction surfaces. These studies are particularly relevant to components in a gas turbine, where minimizing thermal loading can be critical to part life. Of particular relevance is a study by Praisner and Smith [2] which presented time-resolved PIV measurements of vorticity in a plane bisecting the nose of a faired cylinder, correlated with time-resolved contours of surface Stanton number. This study found that two bands of high heat transfer were produced by the unsteady junction flow. The first band was near the leading edge which is caused by fluid flowing down the face of the bluff body leading edge and impinging on the endwall. Another secondary band was upstream of the first band, caused by unsteady eruptive events in which the secondary vortex separated from the endwall, allowing outer region fluid to penetrate to the endwall. While Praisner and Smith [2] provided a good understanding of the effect of unsteady HS vortex behavior on surface heat transfer, the study was done at a freestream Reynolds number based on cylinder diameter of only approximately 2×10^4 , an order of magnitude below that of Devenport and Simpson [4] and below the typical range for gas turbine applications. Unsteady heat flux measurements upstream of the Rood wing by Lewis et al. [5] did not exhibit any bimodal behavior in PDF's in the junction flow region, despite the bimodal flow behavior seen by Devenport and Simpson [4]. Hada et al. [15] replicated the "double-band" heat transfer phenomenon in their study of a wide range of inlet velocities, boundary layer thicknesses, and body thicknesses. They also reported that as the body thickness decreased, the endwall heat transfer increased proportionally. Finally, they also found negligible changes in endwall heat transfer as boundary layer thickness changed.

While much research has already been done on HS vortex dynamics, only a few studies have examined both the HS vortex breakdown dynamics and the associated heat transfer at a range of Reynolds numbers. The study presented in this paper attempts to provide correlated velocity field and endwall heat transfer measurements over a wide range of Reynolds numbers. In addition, the study presents detailed boundary condition information in order to allow for its use in benchmarking advanced numerical studies of the HS vortex.

III. Experimental Setup

A. The Facility

All the experiments for this paper are conducted in a large closed-loop low speed wind tunnel. As shown in Figure 1, the air circulates around the tunnel via a fan, and the flow can be preconditioned by heat exchangers at different stages in the wind tunnel. Also shown in Figure 1 is a newly constructed test section with significant optical access for flow diagnostics. The test section sidewalls as well as the top wall are made of polycarbonate (Lexan), and these walls also have sections where glass is used for optical accessibility. A flow trip as shown in Figure 1 is applied at the start of the boundary layer to ensure a turbulent boundary layer throughout the boundary layer development region. For the current studies, the test section has a boundary layer development length of 2.58 m. The width and height of the test section are 1.12m and 0.55m respectively. Two quarter round shaped geometries ensure a smooth transition into the boundary layer development region.

The test section in Figure 1 houses a single airfoil (Rood wing) at 0° angle of attack. The Rood wing is a research airfoil [4,7] consisting of a 3:2 ellipse nose joined to a NACA 0020 at the maximum thickness point. In Figure 2(a), a symmetric hollow Rood wing with removable nose piece and embedded pressure taps is shown. The dimensions of this geometry are a chord (C) of 40 cm, a span (S) of 54.50 cm, and a maximum thickness (T) of 9.42 cm. The coordinate system origin for this study is at the intersection of the leading edge and endwall, where X is the streamwise direction, Y is the direction normal to the endwall (also parallel to the wing height), and Z is across the tunnel. The Rood wing body is transparent for experimental ease and so that the pressure taps remain visible. The

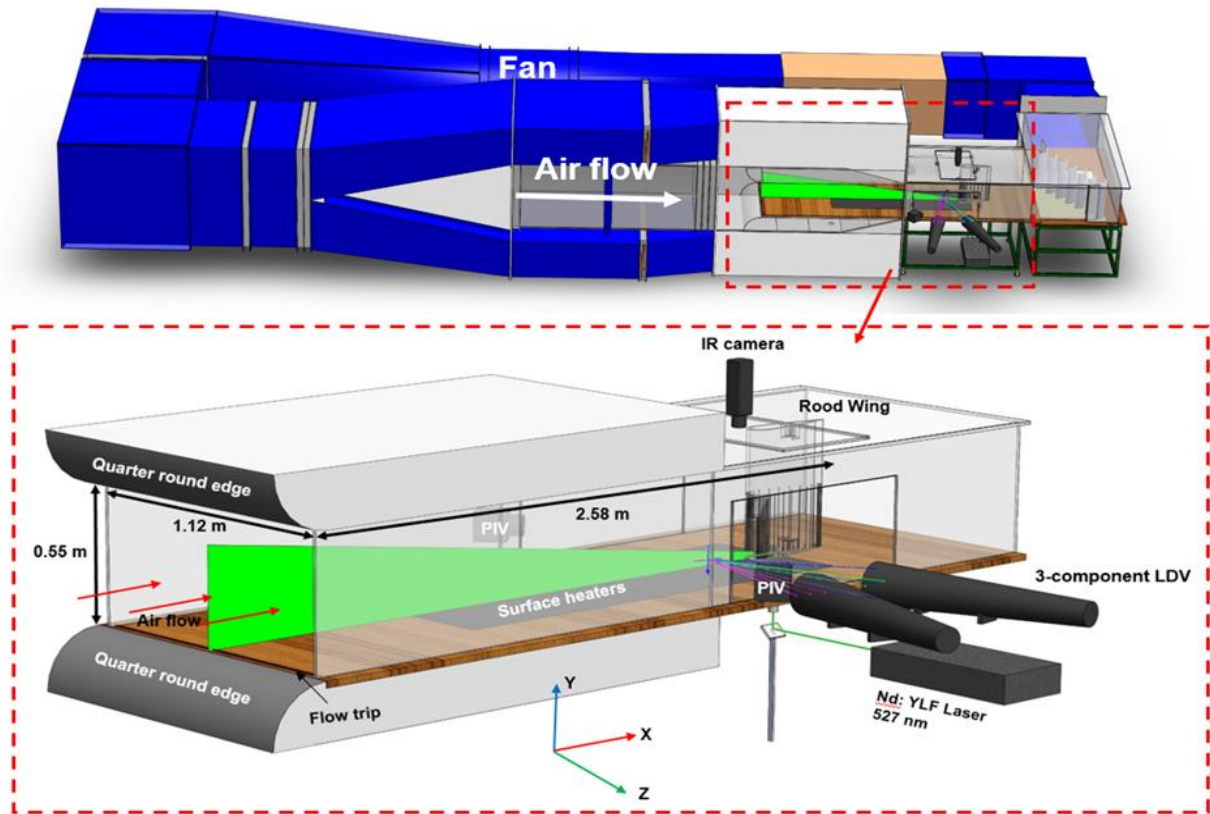


Figure 1. A recirculating low-speed wind tunnel with a new test section to capture junction flow using LDV and SPIV laser diagnostics as well as an IR camera to capture surface heat transfer.

wing is manufactured using a stereolithographic process. The removable nose piece highlighted in Figure 2(a) is made out of polished acrylic so that a laser sheet can be sent through it.

Static pressure taps are located at 50% of the span to check flow symmetry and agreement of the wing pressure distribution with expected behavior in the tunnel. The leading and trailing edges of the Rood wing are intentionally clustered with pressure taps so that flow symmetry and pressure coefficient (C_p) can be determined with higher precision. Figure 2(b) compares measured C_p with time-averaged RANS predictions at 50% span. The x-coordinate is non-dimensionalized by the chord length (C). The C_p measured from the right and left sides of the Rood wing aligns well with time-averaged RANS, confirming flow symmetry around the wing and expected behavior.

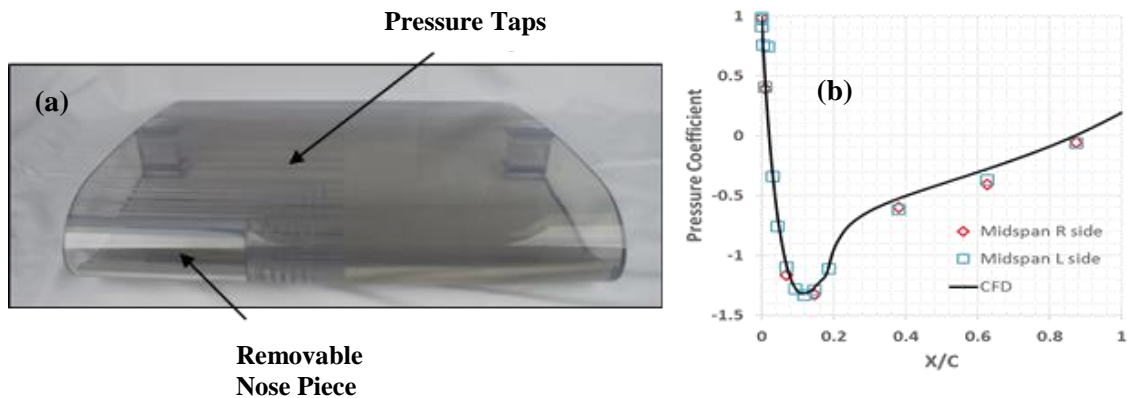


Figure 2. (a) The Rood wing with the leading edge nose piece and built-in pressure taps is shown; (b) the pressure loading around the wing body at 50% span is compared with time-averaged RANS model.

The wing and test section are carefully designed to minimize endwall glare from the laser-based flow diagnostics described later. As shown in Figure 1, the laser output is directed to a 45° mirror under the test section, and then to a series of cylindrical lenses to create a laser sheet, (lenses are not shown in Figure 1 for simplicity), and finally to a second 45° mirror inside the Rood wing. This optical path directs a laser sheet through the leading edge of the wing body along the symmetry plane of the wing, which illuminates the junction flow region for stereo particle image velocimetry (SPIV) measurements. The intensity of the laser sheet near the wall can be controlled to minimize wall reflection.

To capture the flow physics in the junction flow region, two sets of flow diagnostics are available: a three-component laser Doppler velocimeter (LDV) and a stereo particle image velocimetry (SPIV) system. For the current study, only the SPIV is used for the junction flow measurements. Two components of the LDV are used to measure incoming boundary layer velocity profiles. The LDV system consists of a Coherent Innova 70C series argon-ion laser outputting three wavelengths of light into a TSI Fiberlight beam splitter. The beam splitter output is coupled to fiber optic cables to a two-component transceiver probe equipped with a 2.6X beam expander attachment. A TSI PDM 1000 photo detector module along with a TSI FSA 3500 signal processor, all controlled by Flowsizer software are used to acquire measurements. Di-Ethyl-Hexyl Sebecat (DEHS) is used as a tracer particle in the flow. The probe volume is approximately 70 μm in diameter at a standoff distance of 750 mm using the beam expander. Coincident measurements of streamwise and wall-normal velocity are obtained for most of the boundary layer profiles, at sampling rates ranging from 100 Hz very near the wall to 3500 Hz in the freestream. 20,000 data points are obtained for each measurement location to ensure statistical convergence.

The Stereo PIV system includes two Photron FASTCAM Mini UX100 high speed cameras, a Photonics DM20-527 Nd:YLF dual-head laser, and a LaVision timing unit and software control. Images collected are processed using DaVis 8 software. For all cases, the high speed cameras are run at their maximum resolution of 1280x1024 pixels and at a frame rate of 4000 frames per second, or 2000 image pairs (flow samples) per second. For each case, two sets of 4370 image pairs are acquired, (8740 total image pairs, camera memory limited to total of 4370 image pairs at full resolution) taken within 10 minutes of each other at steady state conditions. Because sampling is done with the same sampling rate and image count for all Reynolds numbers, a differing number of flow-through times is captured for each Reynolds number, as can be seen in Table 1. A nondimensional sampling frequency (f_{nd}) is calculated to represent the number of samples per flow-through time, where the flow-through time is determined by the freestream velocity and the size of the measurement window. During data collection, both cameras are fitted with 200 mm focal length lenses and Scheimpflug adapters, for a magnification of 0.04 mm/pixel. Initial calibration of the cameras is done using a LaVision supplied calibration plate, and stereo self-calibration is performed in DaVis after data collection prior to processing to increase stereo reconstruction accuracy. The laser source outputs light at a wavelength of 527 nm with maximum repetition rate of 10 kHz per head, and a maximum output pulse energy of 20 mJ per head. Tracer particles of Di-Ethyl-Hexyl Sebecat (DEHS), with a diameter of approximately 1 micron, are introduced to the flow upstream of the fan so that they are fully mixed in the flow by the time they reach the test section.

Table 1. Summary of flow-through times and nondimensional sampling frequencies

Re_T	6,920	12,600	25,400	47,000	75,000
Flow-through time (sec)	0.128	0.0545	0.0265	0.0140	0.0115
Flow-through Times Captured	34.1	80.1	165	312	316
Nondimensional Sampling Frequency (f_{nd})	256	109	52.9	28.0	23.0

To capture time-averaged convective heat transfer coefficients near the junction flow region, a constant heat flux boundary condition (indicated in Figure 1) is applied using a specially designed serpentine Inconel electric circuit encapsulated in Kapton. A very thin copper layer is adhered to the top surface of the encapsulated Inconel circuit to increase heat flux uniformity, and insulation is placed underneath the circuit to minimize the conduction loss. The heaters are coated with a thin layer of black spray paint to increase surface emissivity with a value of $\epsilon = 0.95$. The temperature difference between surface and freestream is maintained close to 30° C by the heaters. A FLIR A655sc IR camera with 640x480 pixel resolution is mounted above the wing, looking through portholes in the top endwall toward the bottom endwall to capture time-averaged endwall temperatures. Five images are obtained and averaged for each of the seven separate measurement locations around the wing. The images are then calibrated

to embedded thermocouples underneath the heater wall using FLIR software and transformed to airfoil coordinates using an in-house Matlab code.

To calculate surface heat transfer coefficients, the electric power supplied to the circuit is converted to heat flux by dividing by the circuit active area. Conduction (<2%) and radiation losses (~15%) are subtracted to determine convective heat flux. The calibrated surface temperatures from the IR camera, the measured freestream temperature in the tunnel, and the convective heat flux are then used to determine convective heat transfer coefficients.

B. Approach Boundary Layer Parameters

Flowfield and heat transfer measurements are taken with the baseline freestream turbulence level in the tunnel (~1.8%), at five flow speeds corresponding to Reynolds numbers based on wing maximum thickness (T) ranging from approximately 7,000 to 75,000. Table 2 indicates the range of conditions studied along with the measured inlet boundary layer parameters.

Table 2. Summary of experimental cases

U_{ref} (m/s)	1.10	2.01	3.88	7.52	11.95
T (cm)	9.42	9.42	9.42	9.42	9.42
$Re_T = U_{ref}T/\nu$	6,920	12,600	25,400	47,000	75,000
$Re_\theta = U_{ref}\theta/\nu$	550	730	1650	3230	5740
δ/T	0.732	0.541	0.605	0.626	0.700
δ^*/T	0.118	0.082	0.094	0.093	0.104
θ/T	0.079	0.057	0.067	0.069	0.076
C_f	0.00583	0.00513	0.00434	0.00337	0.00300
Tu	2.1%	1.4%	1.7%	1.6%	1.9%

Table 3. Lowest and highest Reynolds number cases from current study are compared with approach boundary layer parameters from previous studies on junction flow

Data set	JLF, WJD1	SCD	HMM	JS	Hada	PS	Current study ($Re_T = 6,920$)	Current study ($Re_T = 75,000$)
Geometry	Rood wing	Rood wing	Rood wing	Rood wing	Cylinder Nose	Faired cylinder	Rood wing	Rood wing
T (cm)	7.17	6.1	7.1	7.1	5.0	15.08	9.42	9.42
U_{ref} (m/s)	26.75	30.5	15.24	20.9	30.0	0.147	1.10	11.95
δ/T	0.513	1.197	0.947	1.15	0.400	0.345	0.732	0.700
δ^*/T	0.0779	0.1345	0.1467	0.148	0.050*	0.047	0.118	0.104
θ/T	0.0548	0.1014	0.1003	0.1227	0.039*	0.037	0.079	0.076
C_f	0.0025	0.0025	0.0023	0.0026	0.0033*	0.0047*	0.00583	0.0030
Re_θ	6,300	11,600	6,800	11,700	3716*	814	550	5740
MDF $*10^{-8}$	7.24	13.3	4.61	11.2	3.56*	0.220	0.037	4.28

(* denotes values that are obtained assuming turbulent boundary layer and associated turbulent correlations.)

Table 3 compares the range of cases in this study to similar studies from previous work. In Table 3, all the datasets except Praisner and Smith as well as Hada et al. used the Rood wing [4,7]. In Table 3, JFL dataset came from Fleming et al., 1991 [16]; SCD dataset came from Dickinson, 1986 a,b [17&18]; HMM was obtained McMahan et al., 1987 [19]; JS was from Shin, 1989 [20]; WJD1 was received from Devenport and Simpson, 1990b and Devenport et al., 1990 [4]; PS is from Praisner and Smith, 2006 [2]; and Haha is from Hada et al, [15]. As seen in Table 3, the current study encompasses a wide range of momentum thickness Reynolds numbers found in other studies, while keeping the ratio of momentum thickness to body relatively constant and in the middle of the range of prior studies.

IV. Data Validation and Uncertainty Analysis

A. Flowfield Validation

Velocity field measurements obtained using Stereo PIV were compared against the LDV measurements of Devenport and Simpson [4] for the highest Reynolds number case tested, $Re_T = 75,000$. This Reynolds number provides a similar magnitude to that of Devenport and Simpson's study on an identical Rood wing geometry (see Table 3 for a comparison of the inlet boundary layer parameters). A comparison of two component (streamwise and wall-normal) turbulent kinetic energy and mean velocity between these two cases is presented in Figure 3. A significant offset in the x-location of the vortex core is visible in Figure 3a between the PIV measurements and Devenport and Simpson's data, with the PIV measurements predicting the vortex core to be approximately $0.04 X/T$ closer to the Rood wing leading edge. A comparison of two-component (streamwise & wall-normal) turbulent kinetic energy is shown in Figure 3a, which demonstrates similar magnitudes of turbulent kinetic energy in the vortex core and a similar shape of the turbulent kinetic energy distribution between the two datasets. In Figure 3b, profiles of the turbulent kinetic energy in a vertical line through the vortex core are compared and show some agreement in the peak turbulent kinetic energy in the vortex core. Near the wall below the vortex core, however, the PIV measurements do not indicate the high values of turbulent kinetic energy shown in Devenport and Simpson's data. This is likely due to the limitations of the PIV system in capturing the very high velocity gradient right at the wall.

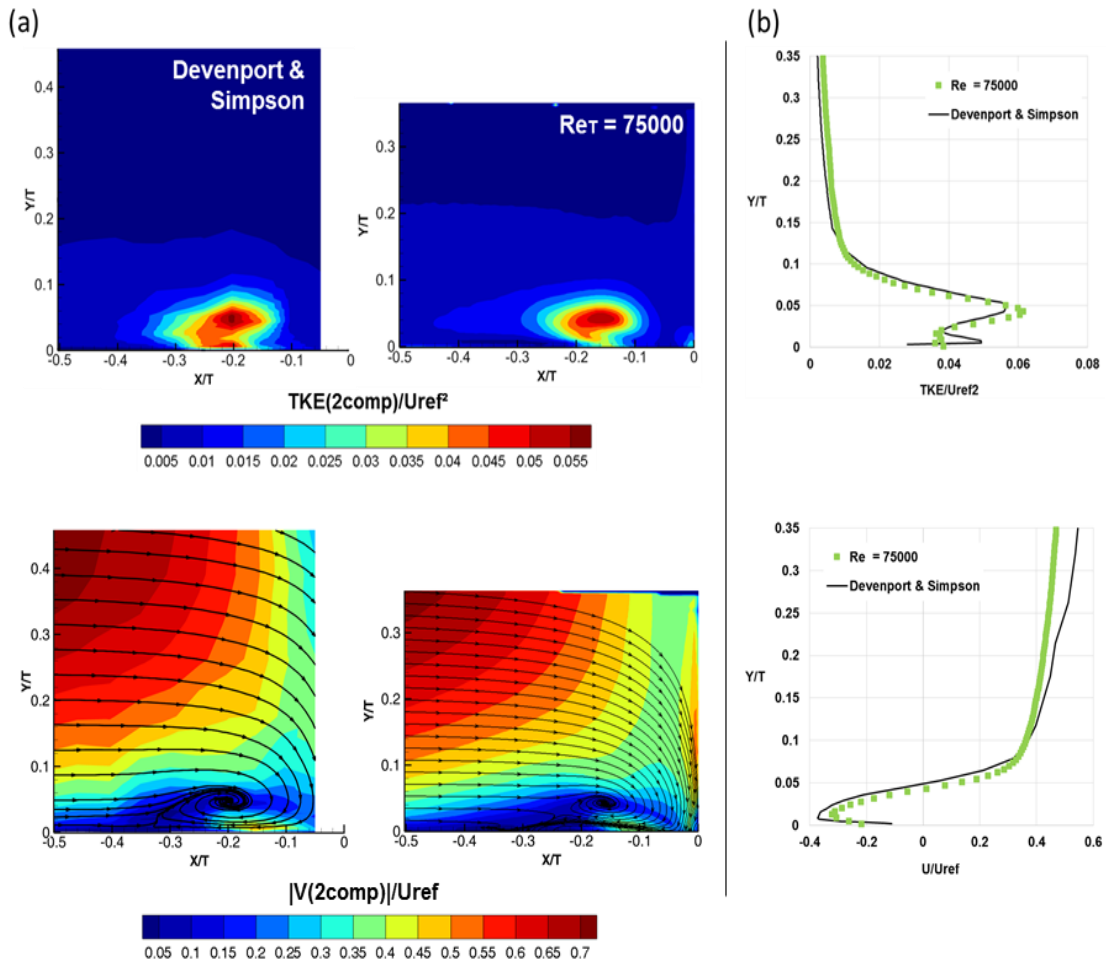


Figure 3. (a) Comparison of two component (u-v) turbulent kinetic energy and mean velocity magnitude contours, and (b) vertical profiles at the time-mean vortex core of two component turbulent kinetic energy and x-direction velocity for $Re_T = 75,000$ compared against Devenport and Simpson [4].

B. Inlet Flow and Heat Transfer Characterization

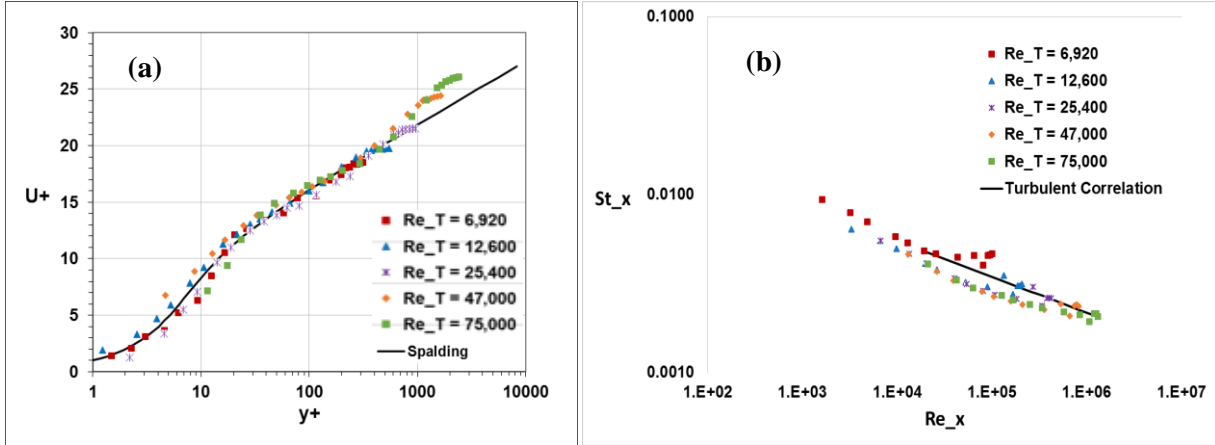


Figure 4. (a) Inlet mean velocity profiles at different Re_T (fixed boundary layer development length); (b) local Stanton numbers (St_x) along the heater upstream of the wing.

Two components of the LDV are used to take inlet mean velocity profiles in all five Re_T cases. The measurements are taken 40.64 cm ($X/C=-1.0$) upstream of the Rood wing leading edge. As seen in Figure 4(a), the inlet mean velocity profiles compare well with the Spalding law of the wall in the log region as expected. Thermocouples are located underneath the endwall heaters from the start of the heating zone to the wing, to capture the development of the endwall heat transfer. Figure 4(b) shows the measured St_x compared with the turbulent Stanton number correlation for a constant heat flux surface. In Figure 4(a & b), Re_T is measured with a fixed body thickness ($T=9.42$ cm) and with changing freestream velocities, and the kinematic viscosity is calculated via measured air density.

C. LDV and PIV Uncertainty

Uncertainty analysis is performed on the Stereo PIV and LDV measurements in this study, showing estimated uncertainty for PIV measurements ranging from approximately 1% near the freestream to 11% in the vortex core, and showing an uncertainty of approximately 5% for LDV measurements. Precision uncertainty is estimated for PIV measurements using four data points sampled from five sets of 4000 images taken under identical conditions using the method described by Moffat [21]. RMS uncertainty in velocity measurements for each of these four locations is reported in Table 4 below. The high degree of uncertainty in the inner core of the vortex and near the bottom wall are likely due to the large gradients in velocity in this region, which is known to be difficult for PIV to accurately capture. LDV precision uncertainty was similarly done by taking multiple points from two separate boundary layer profile measurements (outside the laminar sublayer) to estimate overall error.

Table 4. Uncertainty in PIV measurements at various locations

Location	Non-dimensional Coordinates (X/T, Y/T)	RMS Uncertainty (% with respect to local velocity)	RMS Uncertainty (m/s)	Magnitude of Velocity (m/s)
HS Vortex Center	(-0.145, 0.06)	10.9	0.102	0.940
Outer HS Vortex	(-0.145, 0.08)	5.0	0.0652	1.292
Near Bottom Surface	(-0.15, 0.015)	10.0	0.109	1.088
Near Freestream	(-0.54, 0.34)	0.82	0.0240	2.920

D. Heat Transfer Coefficient Uncertainty

The surface temperatures are measured with thermocouples that have 0.5° biased and 0.26° precision uncertainties. The freestream velocity is measured with 5% uncertainty. The conduction and radiation errors are 2% and 15% respectively and are taken into account when calculating for the local convective heat transfer coefficients (h). The emissivity (ϵ) from the surface is assumed to be 0.95. Heat transfer coefficient (h) is calculated by first measuring the surface temperature at 0.25 m upstream of the Rood wing leading edge. Then, this calculated h is used to find the uncertainty in the local convective heat transfer measurements shown in Figure 5 for the cases studied. The main contribution to the Stanton number uncertainty comes from the uncertainties associated with the measurements of freestream temperature, surface temperature, and surface heat flux.

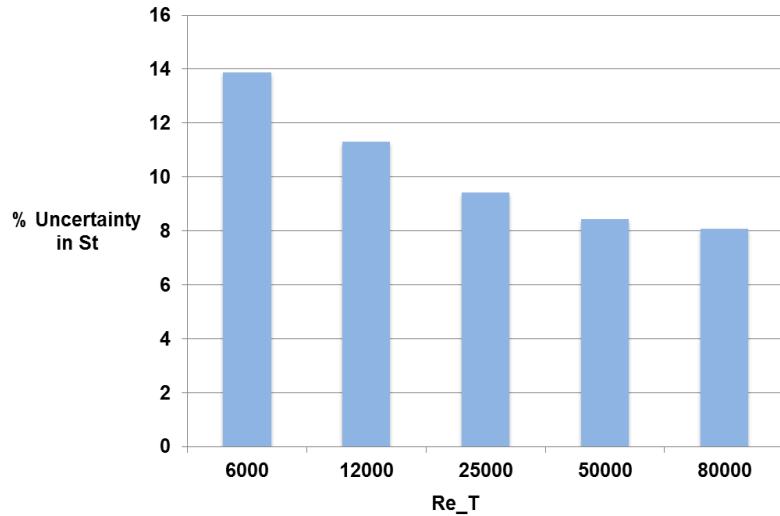


Figure 5. Percent uncertainty in Stanton number shows downward trend with increasing Re_T .

V. Results and Discussion

A. Time Mean Velocity Measurements

An analysis of the time-mean flowfields measured using high speed PIV at varying Reynolds numbers has revealed several key trends in the behavior of the horseshoe vortex with varying Reynolds number. Contours of the three component normalized mean velocity magnitude, turbulent kinetic energy, and the RMS of the fluctuating u-component velocity are provided in Figure 6. The time-mean velocity is typical of other studies, with a large primary vortex that is elliptical-shaped. These results do not indicate strong secondary or tertiary vortices upstream of the primary vortex, as found by some researchers [2,15], although those vortices are also not apparent in the Rood wing results of Devenport and Simpson [4]. The time-mean turbulent kinetic energy is also typical of other studies, with high turbulence in the core of the vortex. A significant contribution to the turbulent kinetic energy is the u-component fluctuations, which are highest right below the time-mean vortex core. This is the region where the intermittent breakdown of the vortex between the backflow and zero-flow modes is occurring most strongly.

Based on the contours of mean velocity magnitude and turbulent kinetic energy in Figure 6, there is no strong trend between the position of the time-mean vortex in the x-direction and the Reynolds number. This conclusion is supported by the earlier findings of Ballio, et al. [14] which also found little effect of Reynolds number on mean core location for a similar range of Reynolds numbers.

Figure 6 indicates some noticeable changes in structure of the mean turbulent kinetic energy within the HS vortex with varying Reynolds number. Underneath the time mean vortex core, turbulent kinetic energy increases near the wall as Reynolds number increases, an effect that is primarily due to an increase in fluctuating velocity in the x-direction near the wall. High turbulent kinetic energy near the wall was also observed at high Reynolds number by Devenport and Simpson [4] and by Escauriaza and Sotiropoulos [12]. Escauriaza and Sotiropoulos [12] also found some evidence of changes to the turbulent kinetic energy underneath the vortex core with Reynolds number; however, they only investigated a small range of Reynolds numbers. The results presented here indicate significant evolution of the high u-rms structure found beneath the vortex as Reynolds number is increased.

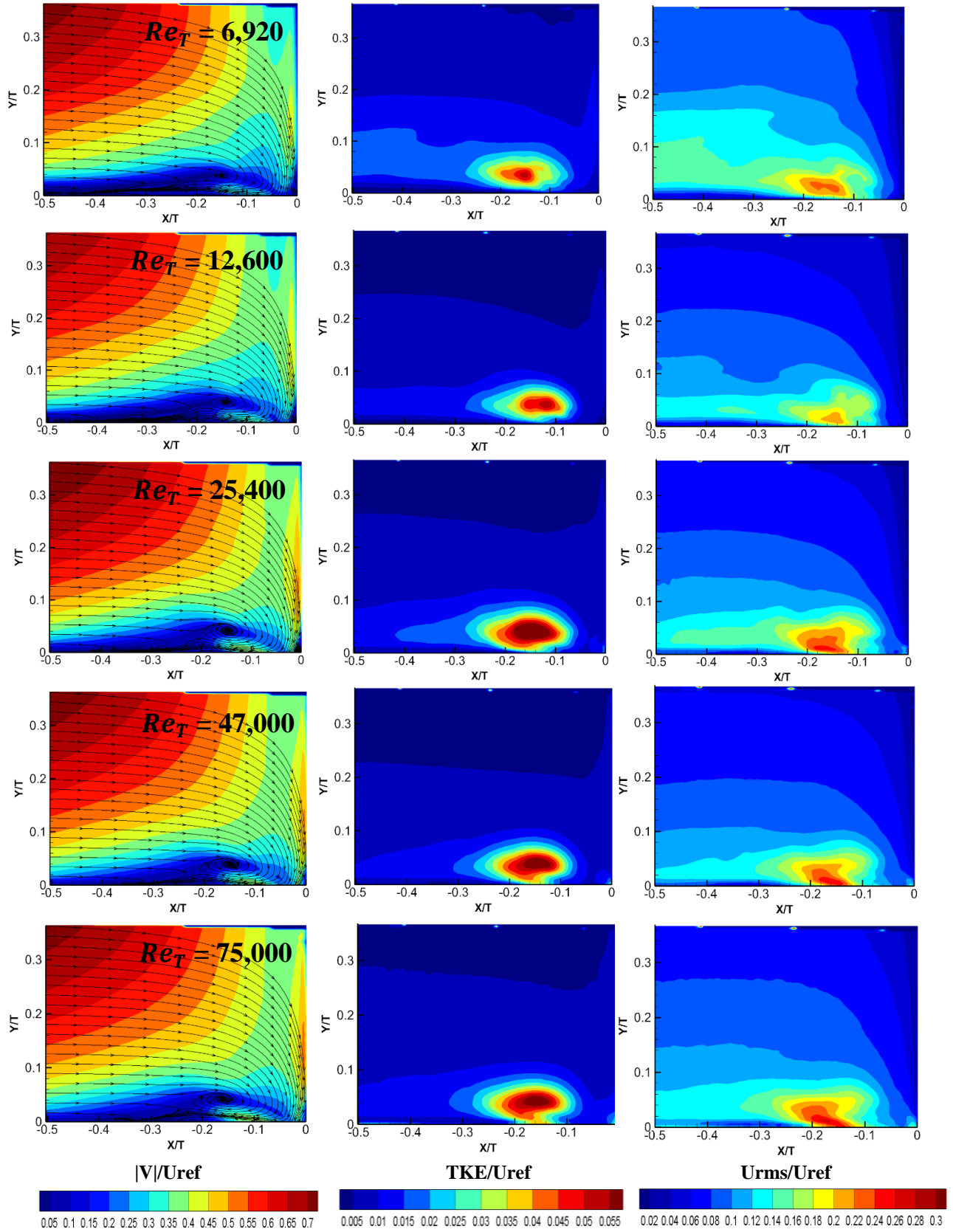


Figure 6. Contours of nondimensional velocity magnitude (left), turbulent kinetic energy (center), and RMS of streamwise fluctuating velocity (right) are given for all Reynolds number cases.

B. Vortex Tracking Analysis

An analysis tool was developed in Matlab to track the instantaneous vortex core to provide additional insight on its movement with varying Reynolds number. The analysis tool computes the instantaneous q -criterion (second invariant of the velocity gradient tensor [22]; $q > 0$ is associated with the swirling component of flow) for each time step and normalizes it so that the maximum in the flowfield is equal to one. It then searches through a specified region in the flow where the HS vortex is known to exist, and extracts the (x,y) coordinates that correspond to a value of normalized q -criterion larger than 0.75. This cutoff is necessary, since in some instances there is no clear vortex feature in the flow during the breakdown events. A search window with dimensions of $-0.3 \leq X/T \leq 0.02$ and $0.005 \leq Y/T \leq 0.2$ is generally sufficient to capture all locations of the vortex position, as observed by watching instantaneous flowfields. A sensitivity analysis of the cutoff value of 0.75 for normalized q -criterion is also performed and indicated negligible changes in the distribution of the instantaneous vortex position, for a range of cutoff values between 0.6 to 0.9. Figure 7 shows output from the tool at two separate time sequences, which correspond to the well-known zero-flow mode and backflow mode of the HS vortex. The red crosshair indicates the instantaneous position of maximum q -criterion, and in the right set of figures, the black line is the prior track of the vortex before the current timestep.

From the instantaneous tracking results, two-dimensional histograms of the vortex core location in x and y space, are given for each Reynolds number tested in Figure 8. The contours shown are of the number of instances per flow-through time recorded for each case, so represent the percent of time that the vortex is located at that position. In general, the histograms are elliptical in shape, with the major axis of the ellipse tilted from vertical. The elliptical shape is due to the bimodal switching phenomenon. For low Reynolds number, the vortex core is more likely to be found in a tight distribution close to the time mean position of the core. For higher Reynolds number, however, the histogram shows a broader distribution of vortex positions in the x -direction away from the time mean core location. The vortex core thus shows a higher likelihood to travel up and downstream from the mean core position within each flow-through time in the higher Reynolds number cases than in the lower Reynolds number cases. This suggests that at higher Reynolds number, the core is less stable and more easily affected by variations in the incoming boundary layer or the freestream. Additionally, it can be observed in the histograms that the highest distribution of instances per flow-through time occur generally in two peak locations for all cases. These positions correspond to the back-flow and zero-flow modes of the horseshoe vortex that have been described by many researchers. In Figure 8, it seems that the spacing between the two modes becomes less distinct with increasing Reynolds number, perhaps due to more frequent perturbations of the vortex by the large range of turbulent scales in the incoming boundary layer as the momentum thickness Reynolds number increases.

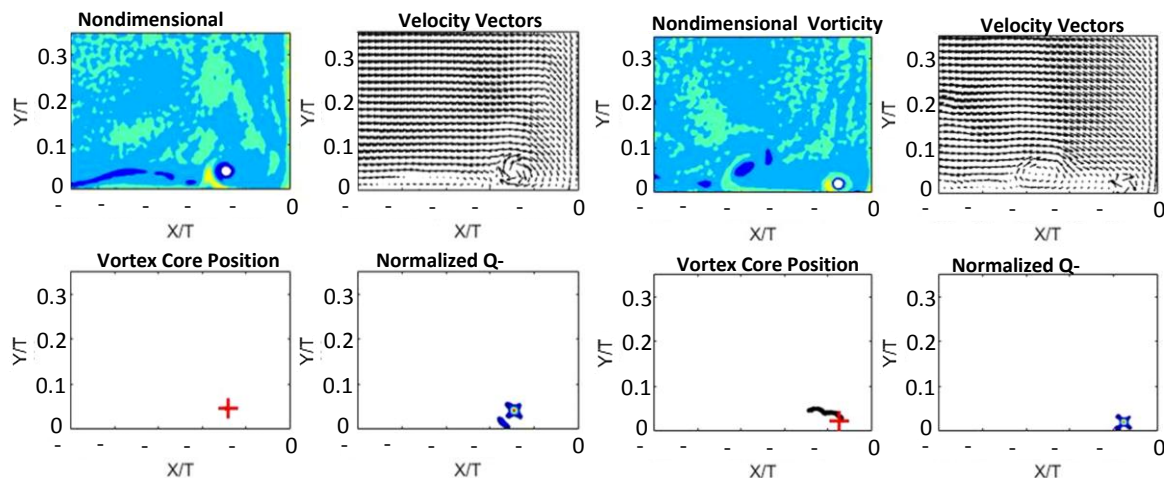


Figure 7. Instantaneous images of the vortex tracking procedure. Shown are contours of vorticity (upper left), u and v vectors (upper right), the vortex tracking scatter plot (lower left), and contours of q -criterion (lower right) for two instants, with the HV in backflow mode (left) and zero flow mode

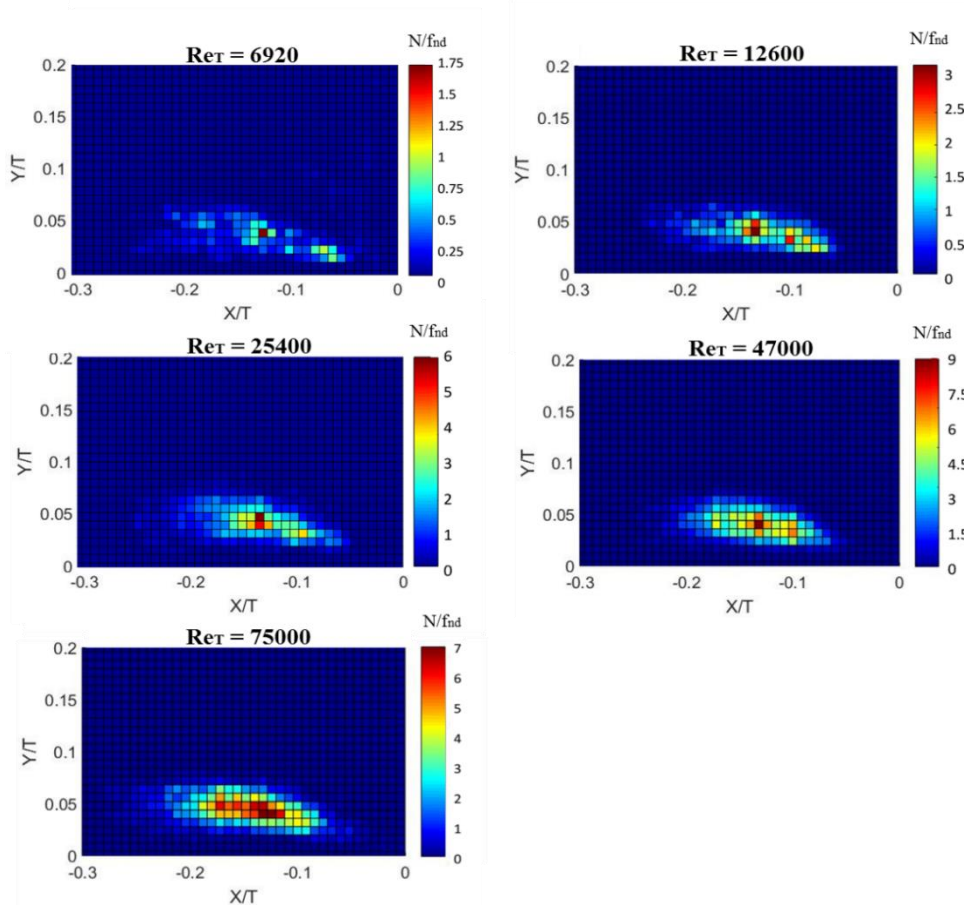


Figure 8. Histograms of number of instances of vortex core position normalized by the nondimensional sampling frequency.

C. Time-Averaged Heat Transfer

Figure 9(a) shows endwall non-dimensional heat transfer coefficient represented in terms of local Stanton number (St) for Re_T of 6,920, 25,400, and 75,000 respectively. Due to the placement of thermocouples underneath the heaters, calibration marks were made on the heaters to indicate their locations for use in calibration and image coordinate transformation. These marks are seen as red isolated spots in the IR images. The lowest Reynolds number case ($Re_T = 6,920$) shows high values of St around the junction flow region. This is caused by the strong swirling motion of the HS vortex in this region. For the highest Reynolds number case ($Re_T = 75,000$), the upstream Stanton number is lower by a factor of 1.5 when compared with $Re_T = 6,920$ case at $X/T = -1$, which is expected since St will decrease with increasing Reynolds number. Unlike other studies of endwall heat transfer [2,15], these results do not indicate a distinct band of high heat transfer away from the junction, which is associated with inrush events between the primary and secondary vortices. The time-average flowfield results in Figure 6, however, do not indicate a distinct secondary vortex for this study, which may be why the high heat transfer band is not apparent in this work.

Figure 9(a) also suggests that the shape of the contours is more full around the leading edge in the low Re_T case compared to the high Re_T case. This is more apparent in Figure 9(b), where the local St for a given case is normalized by the value of St from $X/T = -2.00$ upstream of the leading edge. Around the junction flow region, the normalized St is almost 300% higher than in the upstream turbulent boundary layer, which is corroborated by other studies [2]. The legs of the HS vortex around the sides of the wing, which result in the high heat transfer close to the wing junction, appear to move closer to the wing as Re_T is increased. This may be due to differences in the behavior of the vortex legs where they originate from the symmetry plane; Figure 8 suggests that the average position of the HS vortex is more distinct in the low Re_T case relative to the high Re_T case.

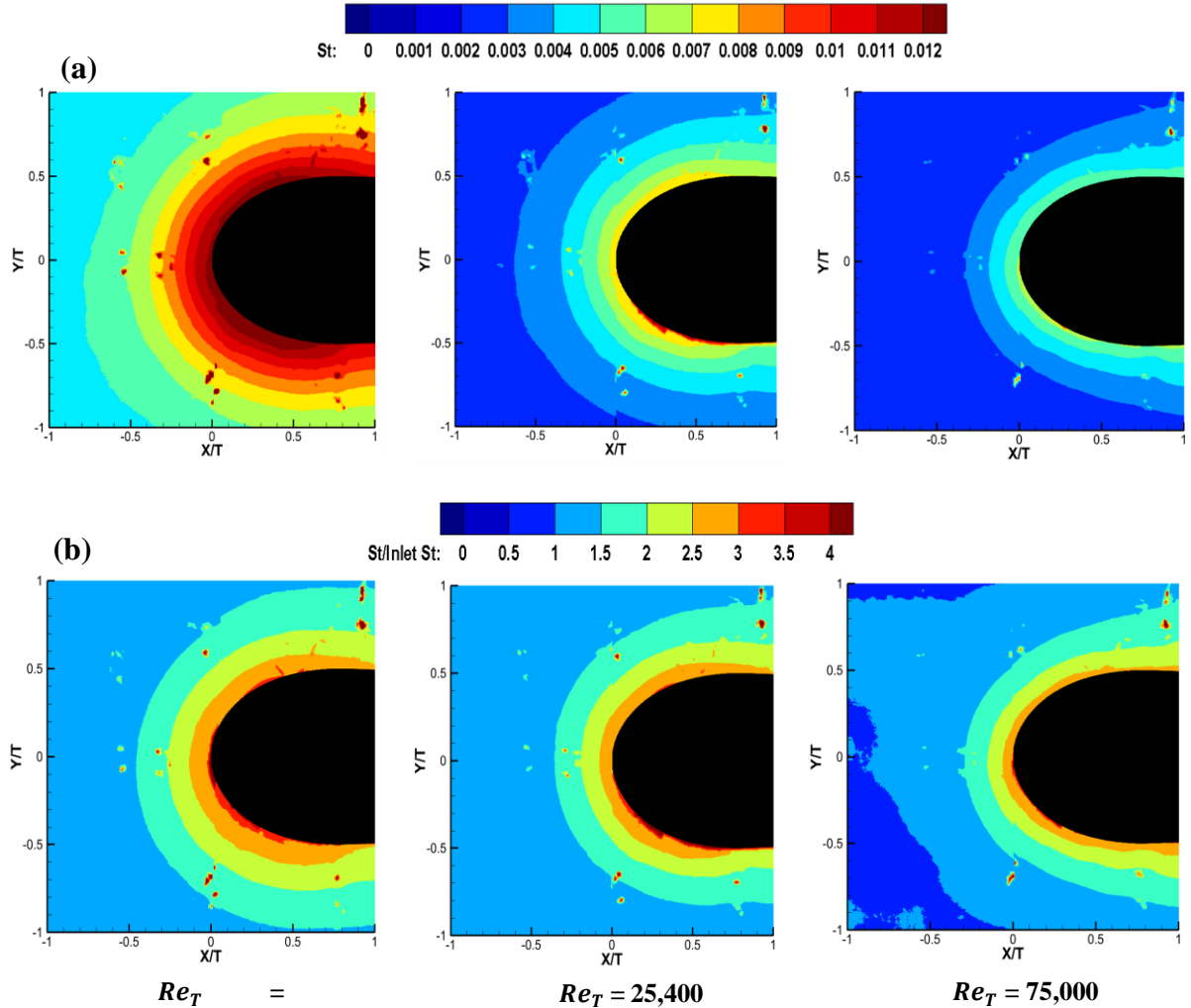


Figure 9. (a) Time-averaged IR images show endwall heat transfer (nondimensionalized as Stanton number) around the Rood wing for three Re_T cases; (b) for same Re_T cases, endwall Stanton number is normalized by inlet Stanton number from $X/T = -2.00$

Figure 10 shows time-averaged normalized z -vorticity in front of the Rood wing leading edge for Re_T of 6,920 and 75,000, overlaid with time-average velocity streamlines. Also, in the same figure, local Stanton number normalized by the inlet ($X/T = -2.00$) Stanton number is shown along the symmetry plane where the flowfield measurements are taken. Both cases show similar nondimensional vorticity in the symmetry plane, which correlates with the similar heat transfer behavior for various Re_T in Figure 9. Paik, et al. [7] points out the very thin layer of positive vorticity underneath the primary opposing vortex core. Both Re_T cases in Figure 10 also show this thin positive vorticity layer underneath the negative vortex core, which Paik, et al. found was a source of the unsteady breakdown initiation. Figure 10 shows that the lowest Re_T case has a slightly more concentrated region of positive vorticity, compared to the highest Re_T case. This may explain why the upstream normalized St is slightly higher in the lowest Re_T case at around $X/T = -0.15$. Note that for both Re_T cases, the time-average streamlines do not indicate strong flow turning toward the wall upstream of the positive vorticity band, which may explain the lack of a second peak in heat transfer that Praisner and Smith [2] described for their cylindrical bluff body.

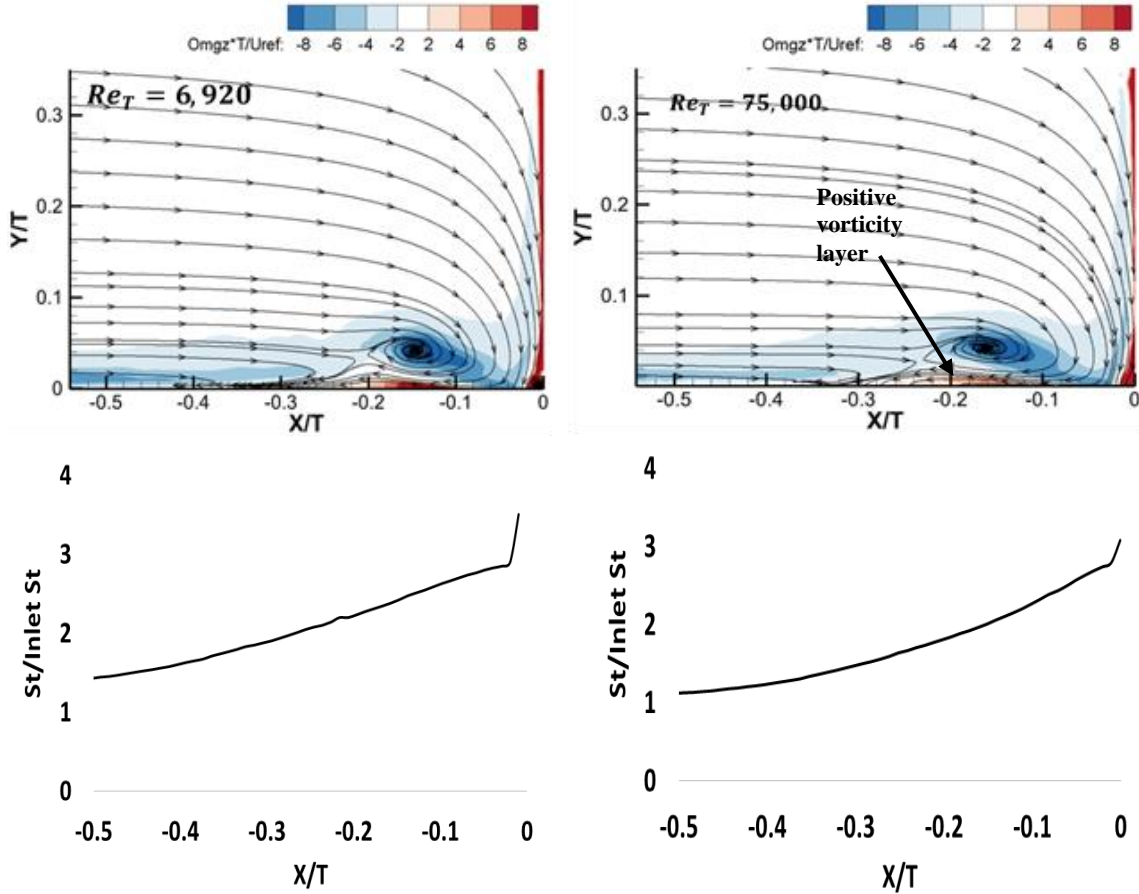


Figure 10. Time-averaged z-vorticity for two extreme Reynolds numbers with time-averaged normalized local Stanton number.

VI. Conclusion

This paper describes a new test rig designed for high speed flowfield measurements and surface heat transfer around the Rood wing research airfoil. Analysis of dynamic flowfield measurements taken using high speed Stereo-PIV support several conclusions in regard to the time-mean and dynamic behavior of the HS vortex within a wide range of Reynolds numbers. Measurements showed that the mean position of the vortex does not significantly change with varying Reynolds number, a conclusion supported by previous studies [12,14]. Additionally, however, time-mean measurements also showed the growth of high turbulent kinetic energy near the bottom wall below the mean vortex core with increasing Reynolds number. This was shown to be largely due to an increase in the relative magnitude of fluctuations in u-velocity in this region for increasing Reynolds number. High Reynolds number has been observed under the HS vortex in previous studies, but to this author's knowledge no study has shown the evolution of this structure from lower to higher Reynolds number. Finally, the use of a newly developed vortex tracking tool identified a larger degree of unsteadiness in the vortex core's position with higher Reynolds number, suggesting the effect of high Reynolds number may lead the vortex to be less stable and more easily perturbed by turbulence in the incoming boundary layer or in the freestream. The time-averaged heat transfer measurements around the Rood wing are also presented in this paper for various Reynolds numbers. The Stanton number contour plots show lowest Reynolds number case to have fuller contours, whereas highest Reynolds number case shows slimmer and compact contours around the wing body.

VII. Acknowledgments

The authors would like to acknowledge assistance from Phil Irwin and Zachary Moul from Penn State University. This work was sponsored by the Office of Naval Research, ONR, under grant number N00014-15-1-2764; the views and conclusions contained herein are those of the authors and should not be interpreted as necessarily representing the official policies or endorsements, either expressed or implied, of the Office of Naval Research, the U.S. Navy or the U.S. government

VIII. References

- [1] Han, J. C., Dutta, S., and Ekkad, S., 2013, Taylor & Francis, New York, NY, USA, Gas Turbine Heat Transfer and Cooling Technology.
- [2] Praisner, T. J., and Smith, C. R., 2006, "The Dynamics of the Horseshoe Vortex and Associated Endwall Heat Transfer---Part I: Temporal Behavior," *Journal of Turbomachinery*, 128(4), pp. 747-754.
- [3] Simpson, R. L., 2001, "Junction Flows," Annual Review of Fluid Mechanics, 33(1), pp. 415-443.
- [4] Devenport, W. J., and Simpson, R. L., 1990, "Time-Dependent and Time-Averaged Turbulence Structure near the Nose of a Wing-Body Junction," *Journal of Fluid Mechanics*, 210(-1), pp. 23-55.
- [5] Lewis, D. J., Simpson, R. L., and Diller, T. E., 1994, "Time-Resolved Surface Heat Flux Measurements in the Wing/Body Junction Vortex," *Journal of Thermophysics and Heat Transfer*, 8(4), pp. 656-663.
- [6] Praisner, T. J., and Smith, C. R., 2006, "The Dynamics of the Horseshoe Vortex and Associated Endwall Heat Transfer---Part II: Time-Mean Results," *Journal of Turbomachinery*, 128(4), pp. 755-762.
- [7] Paik, J., Escauriaza, C., and Sotiropoulos, F., 2007, "On the Bimodal Dynamics of the Turbulent Horseshoe Vortex System in a Wing-Body Junction," *Physics of Fluids (1994-present)*, 19(4), pp. -.
- [8] Yakhot, A., Anor, T., Liu, H., and Nikitin, N., 2006, "Direct Numerical Simulation of Turbulent Flow around a Wall-Mounted Cube: Spatio-Temporal Evolution of Large-Scale Vortices," *Journal of Fluid Mechanics*, 566(pp. 1-9.)
- [9] Apsilidis, N., and Diplas, P., Dancy, C.L., and Bouratsis, P, 2015, "Time-resolved flow dynamics and Reynolds number effects at a wall-cylinder junction," *Journal of Fluid Mechanics*, 776, pp. 475-511.
- [10] Chen, Q., Qi, M., Zhong, Q., and Li, D., 2017, "Experimental study on the multimodal dynamics of the turbulent horseshoe vortex system around a circular cylinder," *Physics of Fluids*, 29, 015106 (2017).
- [11] Kim, S., Walker, D. A., & Simpson, R. L., 1991, "Observation and Measurements of Flow Structures in the Stagnation Region of a Wing-body Junction", Virginia Polytechnic Inst. DTIC document.
- [12] Escauriaza, C. and Sotiropoulos, F., 2011, "Reynolds number effects on the Coherent dynamics of the turbulent horseshoe vortex system," *Flow Turbulence Combust*, 86:231–262 DOI 10.1007/s10494-010-9315-y.
- [13] Fleming, J. L., Simpson, R. L., Cowling, J.E., and Devenport, W. J., 1993, "An Experimental Study of a Turbulent Wing-Body Junction and Wake Flow," *Exp Fluids*, 14, pp. 366-378.
- [14] Ballio, F., Bettoni, C., and Franzetti, S., 1998, "A survey of time-averaged characteristics of laminar and turbulent Horseshoe vortices," *Journal of Fluids Engineering*, 120, pp. 233-242.
- [15] Hada, S., Takeishi, K., Oda, Y., Mori, S., and Nuta, Y., 2008, "The effect of leading edge diameter on the horse shoe vortex and endwall heat transfer," *Proceedings of ASME Turbo Expo 2008: Power for Land, Sea and Air GT2008-50892*.
- [16] Fleming, J. L., Simpson, R. L., and Devenport, W. J., 1991, "An Experimental Study of a Turbulent Wing-Body Junction and Wake Flow," Technical Report No. VPI-AOE-179, Virginia Tech, Virginia Tech, Blacksburg, VA.
- [17] Dickinson, S.C. 1986a: "An experimental investigation of appendage-flat plate junction," vol.1 description. DTNSRDC-86/051.
- [18] Dickinson, S.C. 1986b: "An experimental investigation of appendage-flat plate junction," vol.2 description. DTNSRDC-86/052.
- [19] McMahon, H.M., Merati, P., Yoo, K.M., 1987, "Mean velocities and Reynolds stresses in the junction flow and in the shear layer downstream of an appendage," GITAER 87-4, Georgia Institute of Technology, Atlanta, GA, 30332
- [20] Shin, J., 1989 "Effective methods of controlling a junction vortex system in an incompressible, three-dimensional, turbulent flow," Ph.D Dissertation, Virginia Polytechnic Institute and SU, Blacksburg, VA, 24061
- [21] Moffat, R., 1988, "Describing Uncertainties in Experimental Results", *Experimental Thermal and Fluid Science*, 1:3-17.

- [22] Hunt, J.C.R., Wray, A.A., Moin, P.: “Eddies, Streams, and Convergence Zones in Turbulent Flows”, *Center for Turbulence Research Report CR-S88*, p. 193.
- [23] Anderson, C.D., and Lynch, S.P., 2016, “Time-resolved stereo PIV measurements of the horseshoe vortex system at multiple locations in a low-aspect-ratio pin-fin array,” *Exp Fluids* (2016) 57:5. doi:10.1007/s00348-015-2091-7.